PHYSICAL REVIEW B **101**, 064508 (2020)

Magnetic and superconducting anisotropy in Ni-doped $RbEuFe_4As_4$ single crystals

K. Willa,[1,2] M. P. Smylie,[1,3] Y. Simsek,[1,4] J.-K. Bao,[1] D. Y. Chung,[1] M. G. Kanatzidis,[1,5] W.-K. Kwok,[1] and U. Welp[1]
[1]*Materials Science Division, Argonne National Laboratory, 9700 South Cass Avenue, Lemont, Illinois 60439, USA*
[2]*Institute for Quantum Materials and Technologies, Karlsruhe Institute of Technology, Karlsruhe D-76021, Germany*
[3]*Department of Physics and Astronomy, Hofstra University, Hempstead, New York 11549, USA*
[4]*SUNUM-Sabanci University Nanotechnology Research and Application Center, Istanbul, Turkey*
[5]*Department of Chemistry, Northwestern University, Evanston, Illinois 60208, USA*

(Received 1 August 2019; accepted 8 January 2020; published 10 February 2020)

We investigate the effect of Ni doping on the Fe site in single crystals of the magnetic superconductor $RbEuFe_4As_4$ for doping concentrations of up to 4%. A clear suppression in the superconducting transition temperature is observed in specific-heat, resistivity, and magnetization measurements. Upon Ni doping, the resistivity curves shift up in a parallel fashion, indicating a strong increase of the residual resistivity due to scattering by charged dopant atoms while the shape of the curve and thus the electronic structure appear largely unchanged. The observed step $\Delta C/T_c$ at the superconducting transition decreases strongly for increasing Ni doping in agreement with expectations based on a model of multiband superconductivity and strong interband pairing. The upper critical field slopes are reduced upon Ni doping for in-plane as well as out-of-plane fields, leading to a small reduction in the superconducting anisotropy. The specific-heat measurements of the magnetic transition reveal the same Berezinskii-Kosterlitz-Thouless behavior close to the transition temperature T_m for all doping levels. The transition temperature is essentially unchanged upon doping. The in-plane to out-of-plane anisotropy of Eu magnetism observed at small magnetic fields is unaltered as compared to the undoped compound. All of these observations indicate a decoupling of the Eu magnetism from superconductivity and essentially no influence of Ni doping on the Eu magnetism in this compound.

DOI: 10.1103/PhysRevB.101.064508

I. INTRODUCTION

The family of iron-based superconductors has been constantly growing, now comprising many members of the so-called 11, 111, 1111, and 122 materials [1–9]. In the majority of these materials, superconductivity arises from an antiferromagnetic parent compound upon electron, hole, or isovalent doping or mechanical pressure [1,2,4–14]. The so-called 1144 compounds with composition $AAeFe_4As_4$ ($A =$ K, Rb, Cs; $Ae =$ Ca, Sr, Eu) [15–19] form the most recently discovered members of this family. In these materials, the large difference in the ionic radii of the A and Ae atoms leads to the formation of alternating A and Ae layers between the Fe_2As_2 planes producing an asymmetric environment for the Fe_2As_2 layers. Contrary to the doped 122 compounds, the 1144 compounds are superconducting in their stoichiometric state with T_c reaching ≈37 K. A formal charge count yields that stoichiometric 1144 are intrinsically hole doped to ≈0.25 holes/Fe, close to the doping level that yields optimum T_c in the 122 compounds. Recently, it has been realized [20] that the high-purity and symmetry properties of 1144 materials such as $CaKFe_4As_4$ may open a new platform for the observation of topological band structures and Majorana zero modes.

The $AEuFe_4As_4$ compounds represent a peculiar subgroup of this new family as they exhibit the coexistence of unconventional magnetism and superconductivity over a large temperature range. Initial experiments on polycrystalline $RbEuFe_4As_4$ samples indicated magnetic order at 15 K, deep within the superconducting phase ($T_c = 37$ K) [17,18]. Studies on single crystals [21] affirmed these findings and allowed for the study of the magnetic and superconducting anisotropy [22,23], demonstrating a low superconducting anisotropy of 1.8, highly anisotropic quasi-two-dimensional (quasi-2D) Eu magnetism, and an associated Berezinskii-Kosterlitz-Thouless (BKT) transition of the Eu^{2+} moments. Large upper critical fields were observed in pulsed field measurements [24]. While Eu layers are ordered ferromagnetically as in the $EuFe_2As_2$ [25–29], recent neutron and x-ray scattering data on $RbEuFe_4As_4$ revealed an unconventional helical magnetic stacking of the Eu layers accompanied by a 90° layer-to-layer turn, resulting in a commensurate helix with a period of four c-axis lattice constants [30,31].

Furthermore, a study on polycrystalline samples [32] revealed that T_c is suppressed upon Ni substitution on the Fe site, while the magnetic ordering temperature is unchanged. Meanwhile, Ca substitution on the Eu site [33] suppressed the magnetic ordering temperature in polycrystalline samples without changing T_c. These results and recent high-pressure studies [34] suggest an almost complete decoupling of superconductivity hosted by the Fe_2As_2 planes and magnetism within the Eu layers. Nevertheless, theoretical analysis [35,36] indicates that it is the coupling of magnetism and superconductivity that gives rise to the helical magnetic structure, as well as to the occurrence of self-induced superconducting critical states [37]. Therefore, $RbEuFe_4As_4$ and related compounds provide an ideal platform to selectively tune the relative importance of magnetism and superconductivity, rendering these compounds promising for further investigations of new aspects of the interplay of magnetism and superconductivity.

Here, we present a systematic study of the evolution of the superconducting and magnetic transitions and of the normal-state magnetotransport of single-crystal RbEu($Fe_{1-x}Ni_x$)$_4$As$_4$. We find that upon Ni doping the residual resistivity strongly increases while the electronic structure appears largely unchanged. Notwithstanding increased electron scattering, the upper critical field slopes for in-plane as well as out-of-plane fields are reduced resulting in a small overall reduction in the superconducting anisotropy. The BKT nature of the magnetic transition is not affected by Ni doping. The anomaly of the specific heat at T_c decreases strongly with Ni doping, reminiscent of the BNC scaling [38,39]. Taken together with the transport data, these results underscore the importance of multiband effects in determining the thermodynamic properties of RbEuFe$_4$As$_4$.

II. EXPERIMENTAL METHODS

High-quality single crystals RbEu($Fe_{1-x}Ni_x$)$_4$As$_4$ were grown out of RbAs flux with a similar method to the one used for the undoped RbEuFe$_4$As$_4$ in Ref. [21]. In order to provide the Ni doping, an extra NiAs precursor was synthesized by reacting Ni and As powder under a 1:1 ratio in an evacuated quartz tube at 823 K for 12 h. The sintered NiAs precursor was then ground into a fine powder in an agate mortar. To achieve a nominal Ni doping x ($x = 0.03$, 0.05, 0.07), EuAs:Fe$_2$As:NiAs:RbAs $=$ 1:1-x:2x:15 were used for the RbAs flux growth. After the growth, the RbEu($Fe_{1-x}Ni_x$)$_4$As$_4$ crystals were obtained by removing the RbAs flux with reagent alcohol. This procedure yields thin flat plates with typical sizes of $300 \times 300 \times 50\ \mu\text{m}^3$, with the tetragonal [110] and [$1\bar{1}0$] orientations parallel to the long edges, and the [001] orientation perpendicular to the plate.

We performed x-ray diffraction (XRD) measurements on single crystals using a powder x-ray PANalytical diffractometer X'pert with a Cu-K_α source. Platelike crystals were well oriented in a flat zero-background single-crystalline silicon sample holder to make sure that peaks with the index (00l) were observed (see Fig. 1). Magnetization measurements were performed in a Quantum Design MPMS-7 system with samples mounted in a notched quartz rod for $H \parallel [001]$ and on a smooth quartz rod for $H \parallel [110]$. For low-field measurements, careful background field calibration was performed prior to each run with a Pd reference sample. For magnetotransport measurements, four-bar gold patterns were deposited onto thin rectangular-shaped crystals with the help of a shadow-mask technique, then thin gold wires were attached onto the gold bars with silver epoxy. The measurements were performed inside a $9-1-1$ T three-axis AMI superconducting vector magnet in a four-point geometry with DC currents of 1 mA applied along the in-plane direction. The AC specific heat was measured on a SiN calorimetric membrane [40,41]. For this purpose, a small ($\approx 100 \times 100 \times 25\ \mu\text{m}^3$) platelet-shaped single crystal was mounted on the nanocalorimeter platform with apiezon grease and inserted into the same three-axis superconducting vector magnet as used for resistivity measurements. The sample was then subjected to a small oscillatory heating current with frequencies usually in the range of 1 Hz and the response of the sample was measured using a SynkTek MCL1-540 multichannel lock-in system.

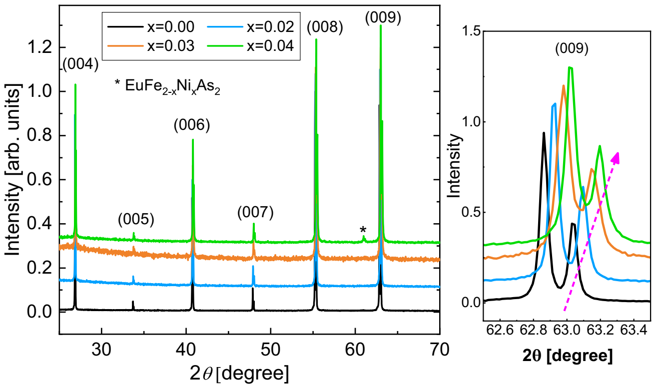

FIG. 1. XRD measurements of (00l) peaks on single-crystal RbEu($Fe_{1-x}Ni_x$)$_4$As$_4$ for $x = 0.00$ (black), $x = 0.02$ (blue), $x = 0.03$ (orange), $x = 0.04$ (green). As doping increases, the lattice peaks systematically shift to higher angles as the lattice shrinks; compare Table I. The inset shows the (009) peak. The asterisk marks a small amount of 122-phase compound that grows at the surface of the 1144 phase. No other phases have been observed.

III. EXPERIMENT

A. Diffraction

We used energy-dispersive x-ray spectroscopy (EDS) to determine the actual Ni content of the RbEu($Fe_{1-x}Ni_x$)$_4$As$_4$ single crystals. For this, about 10 crystals from each doping series were investigated. We found that the nominal doping concentrations of $x = 0.03$, 0.05, and 0.07 correspond to an actual doping concentration of $x = 0.02$, 0.03, and 0.04, respectively; from here on, samples will be referred to by their average EDS doping values. The spread of doping concentrations in any batch is around $\pm 0.1\%$. In XRD measurements using Cu-$K\alpha_1$ radiation we observe (00l) peaks of the of the single-crystal RbEu($Fe_{1-x}Ni_x$)$_4$As$_4$ with doping levels of $x = 0.00$ (black), $x = 0.02$ (blue), $x = 0.03$ (orange), $x = 0.04$ (green), as shown in Fig. 1. With increasing doping, the lattice peaks systematically shift to higher angles [see inset of Fig. 1 where the (009) peak is shown]. This indicates a shrinking of the c-axis lattice constant.

We determine the c-axis lattice parameter from least-squares fits with a zero-shift parameter of all observed peaks as shown in Fig. 1. We estimate the uncertainty to be less than 7×10^{-4} Å. A few samples show a small amount of nonsuperconducting Eu122-impurity phase that grows on the surface of the RbEuFe$_4$As$_4$ crystals. No other impurity phases were observed. The c axis decreases almost linearly with increasing Ni doping at a rate of $\approx -8 \times 10^{-3}$ Å/% Ni which is in good agreement with low-doping data on polycrystalline samples [32] and is consistent with Vegard's law implying the uniform incorporation of Ni.

B. Resistivity

Figure 2 shows the temperature dependence of the in-plane electrical resistivity ρ_{ab} of single crystals of

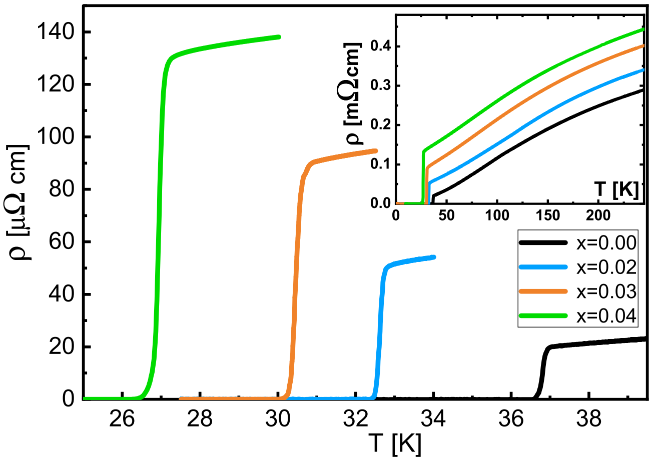

FIG. 2. Resistivity as a function of temperature of single crystals of RbEu$(Fe_{1-x}Ni_x)_4As_4$ with current in plane. As the doping increases, the normal-state resistivity increases (see inset) and the transition temperature decreases. Qualitatively, the temperature dependence of the resistivity remains unchanged.

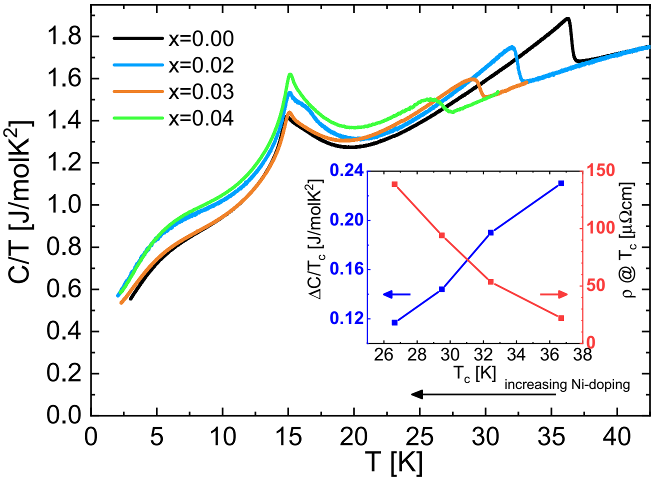

FIG. 4. Temperature dependence of C/T of RbEu$(Fe_{1-x}Ni_x)_4As_4$ in zero field. A clear step marks the onset of superconductivity, while the magnetic transition of the Eu moments is seen as a kink around $T_m = 15$ K.

RbEu$(Fe_{1-x}Ni_x)_4As_4$ at different doping levels. The superconducting transition temperature T_c is clearly suppressed upon increasing Ni doping at a rate of ≈ -2.4 K/%Ni, consistent with the polycrystalline data at low Ni doping [32]. In all samples, the resistive transitions remain sharp with a transition width below 0.5 K, indicating uniform doping and single-phase material. As seen in the inset of Fig. 2, the salient effect of Ni doping is the remarkable parallel upward shift of the resistivity curve. The resistivity at T_c vs T_c can be seen in the inset of Fig. 4. While the residual resistivity increases

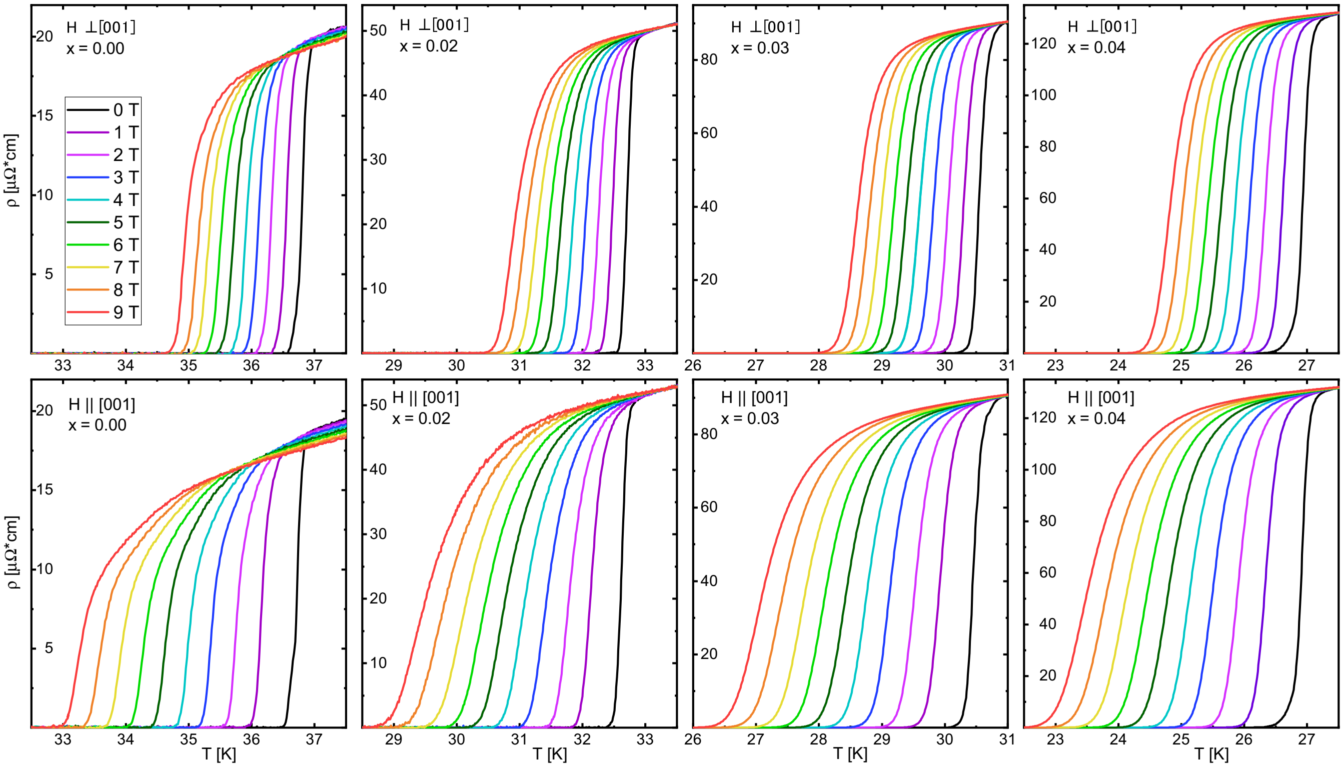

FIG. 3. Temperature dependence of the resistivity of RbEu$(Fe_{1-x}Ni_x)_4As_4$ in in fields of up to 9 T. Upper panels are for fields in plane, lower panels for fields along the c axis. The color code is the same for all panels. For all doping levels, the superconducting transition is suppressed and broadens with increasing fields, more for fields along the c axis than for in-plane fields. The suppression with fields gets larger for increasing Ni doping. The temperature axis of all panels spans 5 K, whereas the vertical axis is adjusted to accommodate the large increase in resistivity with doping.

strongly, the temperature dependence of the resistivity is not altered. In particular, an upturn (on decreasing temperature) of the resistivity, which was observed around 30 K on polycrystalline samples [32] at doping levels of 3% and above and interpreted as the reemergence of the spin density wave on Fe, is not apparent in our data. As electron scattering by phonons as well as spin fluctuations depend on the details of the electronic band structure, our results imply that the effects of doping-induced changes of the band structure on electron transport are small. Recent first-principles calculations [42] of the electronic properties of Ni-doped $\mathrm{RbEuFe_4As_4}$ revealed that Ni doping induces electron doping accompanied by an upward shift of the Fermi energy. For 6.25% Ni, the partial density of states derived from the Fe-$d_{x(y)z}$, d_{z^2}, and $d_{x^2-y^2}$ orbitals were found to decrease by approximately 10% to 20% while for the d_{xy} states it increases by 4%. Since T_c depends exponentially on the density of states, these small changes result in a clear suppression of T_c. In contrast, the resistivity depends much more weakly on the density of states, and the large observed increases of the resistivity are attributable to enhanced disorder scattering due to the charged Ni dopants. For all doping levels, we do not observe a reentrant resistive state associated with the onset of Eu sublattice magnetic order; this is in agreement with earlier reports on the polycrystalline material [32] but in contrast to other Eu-containing iron-based superconductors, e.g., $\mathrm{Eu(Fe_{1-x}Ir_x)_2As_2}$ [43].

Figure 3 shows the superconducting transitions of the pristine and doped samples in in-plane (top row) and out-of-plane fields (bottom row). For all samples, the field-induced suppression and broadening of the superconducting transition is stronger for fields along the c axis than for in-plane fields and also increases for increasing Ni content, yielding a modest superconducting anisotropy of 1.8 in the pristine sample which slightly decreases upon Ni doping (see below, Fig. 7). The superconducting transition temperature as a function of field was extracted as the midpoint of the transition and is used to construct the phase boundaries, which can be seen in Fig. 7. The high-field transitions of the pristine sample are characterized by an unusual sharpening on decreasing temperature, clearly seen in the 9-T $\parallel c$ R-T curve. This feature is associated with the vortex lattice melting transition [44] and is suppressed due to the increased disorder in the doped samples. Furthermore, the negative normal-state magnetoresistance that is clearly seen in the pristine sample (see also Ref. [22]) is strongly reduced with increasing Ni doping, consistent with the increase in impurity scattering.

C. Specific heat

Figure 4 shows the zero-field specific heat of the pure $\mathrm{RbEuFe_4As_4}$ and for the three different Ni-doping levels. Due to the small sample size, the determination of the molar volume for each sample introduces uncertainties. Therefore, in order to facilitate the comparison of the data from different samples, we scale the normal-state molar specific heat of the Ni-doped samples to the normal-state specific heat of the pure $\mathrm{RbEuFe_4As_4}$ compound. This step is motivated by the observation that substituting Fe by Ni induces essentially no change in the lattice specific heat and very little in the normal-state electronic specific heat. The two clear features in C/T are (i) a step signaling the superconducting phase transition at T_c and (ii) a kink at the magnetic transition temperature T_m while the superconducting transition temperature is clearly suppressed, both in temperature and in step-height; upon increasing Ni doping, the shape and transition temperature T_m of the magnetic transition change only weakly. Even for the largest Ni concentrations investigated here, the Eu moments order below the superconducting transition. Consistent with the resistivity data, there is no additional feature in the specific heat between 2 K and room temperature which would indicate a spin-density wave (on the Fe site) as is seen in most 122 parent compounds [3–9,26,29,45].

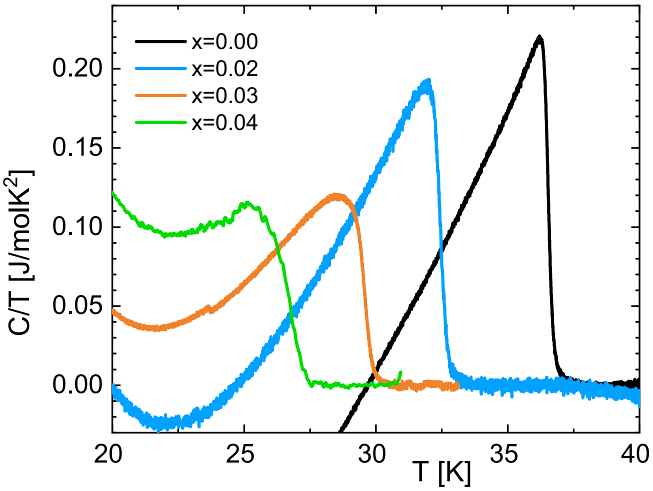

FIG. 5. Specific heat of the superconducting transition of $\mathrm{RbEu(Fe_{1-x}Ni_x)_4As_4}$ for different doping levels. A linear normal-state background has been subtracted. The step height of the jump in C/T decreases with increasing Ni concentration from 0.23 J/mol K^2 down to 0.12 J/mol K^2. The observed upturn of C/T at around 23 K is due to magnetic fluctuations.

Figure 5 shows the superconducting contribution to the specific heat of the four samples obtained by subtracting a linear extrapolation of the normal-state data above T_c. The transition temperature decreases from $T_c = 36.9$ K for the undoped compound to $T_c = 26.7$ K for 4% Ni doping. While the step height is reduced from 0.23 J/mol K^2 to 0.12 J/mol K^2. The evolution of the step size with Ni doping can be seen in inset of Fig. 4. In single-band weak-coupling BCS theory, the specific-heat anomaly is given as $\Delta C/T_c = 1.43\gamma_n$, where γ_n is the Sommerfeld coefficient of the electronic specific heat. Thus, the rapid suppression of $\Delta C/T_c$ with Ni doping would indicate a strong reduction in the density of states, contrary to the transport data (see above). Alternatively, however, a strong dependence of $\Delta C/T_c$ on T_c has been observed in a wide variety of iron-based superconductors, a phenomenon known as the BNC scaling [38]. It is believed that this behavior arises in multiband superconductors with strong interband pairing interaction [39] and thus might be responsible for the strong reduction in $\Delta C/T_c$.

Figure 6 shows C/T of the three Ni-doped samples in fields of up to 9 T applied along the c axis. In analogy to the magnetotransport data in Fig. 3, with increasing fields, the superconducting transition is suppressed and broadened.

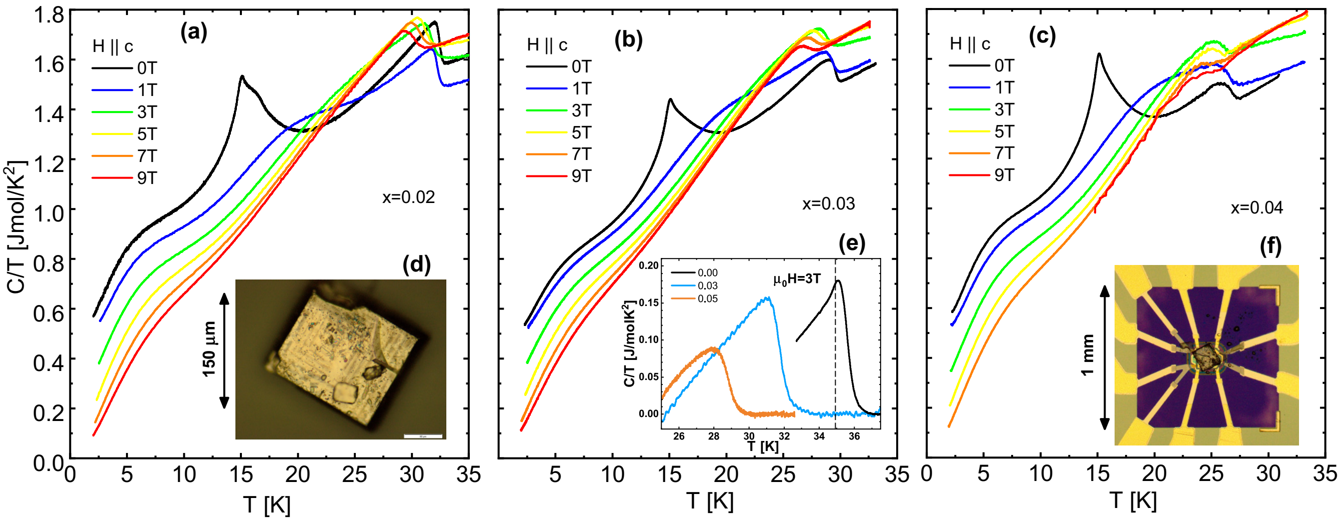

FIG. 6. C/T versus temperature for the three different Ni concentrations $x = 0.02$ (a), $x = 0.03$ (b), and $x = 0.04$ (c). Fields of up to 9 T were applied along the c axis suppressing the superconducting transition. The broadening of the transitions in field is considerably larger for higher Ni doping. The magnetic transition is transformed into a broad hump that moves to higher temperatures with fluctuations extending well above the superconducting transition. The insets (d) and (f) show a 2%- and 4%-doped $\mathrm{RbEu(Fe_{1-x}Ni_x)_4As_4}$ single crystal, respectively. Inset (e) shows C/T (normal-state background subtracted) measured in 3 T for 0%, 2%, and 3% Ni doping. In the pristine sample, the additional step below T_c (marked by a dotted line) indicates the vortex lattice melting. This is not visible anymore for the higher doped samples.

The broadening in field is considerably larger for the higher doped samples. At the same time, the magnetic transition transforms from a kink into a crossover that moves to higher temperatures in increasing field. The associated specific-heat contribution due to strong magnetic fluctuations persists far above the superconducting transition. Previous specific-heat measurements on pristine $\mathrm{RbEuFe_4As_4}$ revealed a step in C/T slightly below the superconducting transition [44] that lines up with the steep drop in the resistance and is a signature of the vortex lattice melting transition. Inset (e) of Fig. 6 shows C/T (normal-state background subtracted) measured in 3 T for 0%, 2%, and 3% Ni doping. In the pristine sample, the additional step below T_c (marked by the dotted line) indicates the vortex lattice melting. Upon Ni doping, this feature is suppressed due to increased impurities and pinning sites in the sample which is consistent with the evolution of the magnetoresistance.

We have extracted the superconducting phase boundaries of the superconducting transition using an entropy-conserving construction [46] and plotted it together with those obtained from resistive midpoints and magnetization (see Fig. 7). The agreement between resistivity and specific-heat derived data is generally good. The difference in T_c for the 3% sample can be attributed to measurements on crystals from different batches having slightly different doping levels. The upper critical field slopes dH_{c2}/dT for both in-plane and out-of-plane fields are suppressed with increasing Ni doping. Taking the resistivity data, we observe that the c-axis upper critical field slope decreases from around 4 T/K for the undoped sample to 3.3 T/K for 4% doping, whereas the in-plane direction changes from 6.3 T/K ($x = 0.00$) to 5 T/K ($x = 0.04$). This results in a small reduction of the superconducting anisotropy from $\Gamma = (dH_{c2}^{ab}/dT)/(dH_{c2}^{c}/dT) = 1.6$ to $\Gamma = 1.5$. Naively, one would expect that with increasing disorder, as is suggested by the strong increase of the residual resistivity, the upper critical fields H_{c2} and dH_{c2}/dT increase as the coherence length decreases. However, T_c decreases also with Ni doping. Since our data are taken close to T_c, we present simple estimates using the Ginzburg-Landau formalism giving $H_{c2}(T) = \Phi_0/2\pi\xi^2(T)$. In the clean limit, $\xi(0) < l = v_F\tau$ with l, v_F, and τ the electron mean-free path, the Fermi velocity, and scattering time, respectively, the coherence length is given by

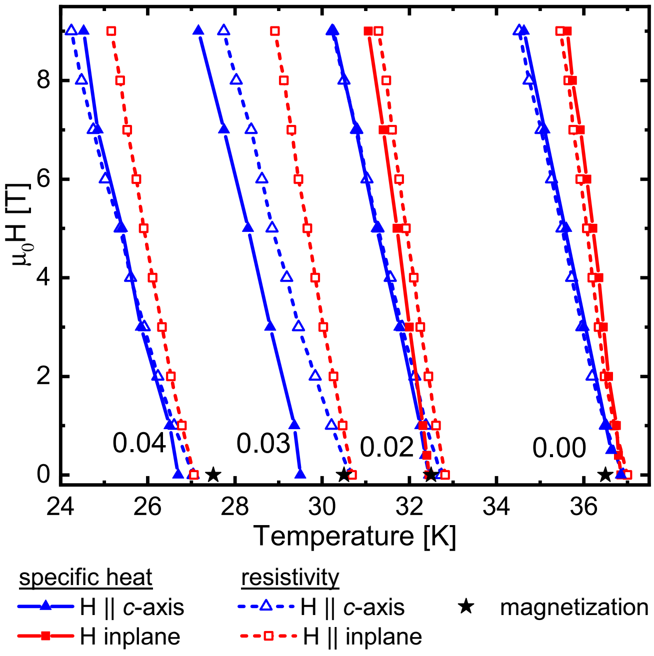

FIG. 7. Phase boundary of pure and Ni-doped $\mathrm{RbEuFe_4As_4}$ single crystals for in-plane and out-of-plane fields. Data are obtained from resistivity (open symbols and dashed lines) and specific heat (closed symbols and solid lines). The superconducting transition obtained from susceptibility measurements is indicated as well (stars).

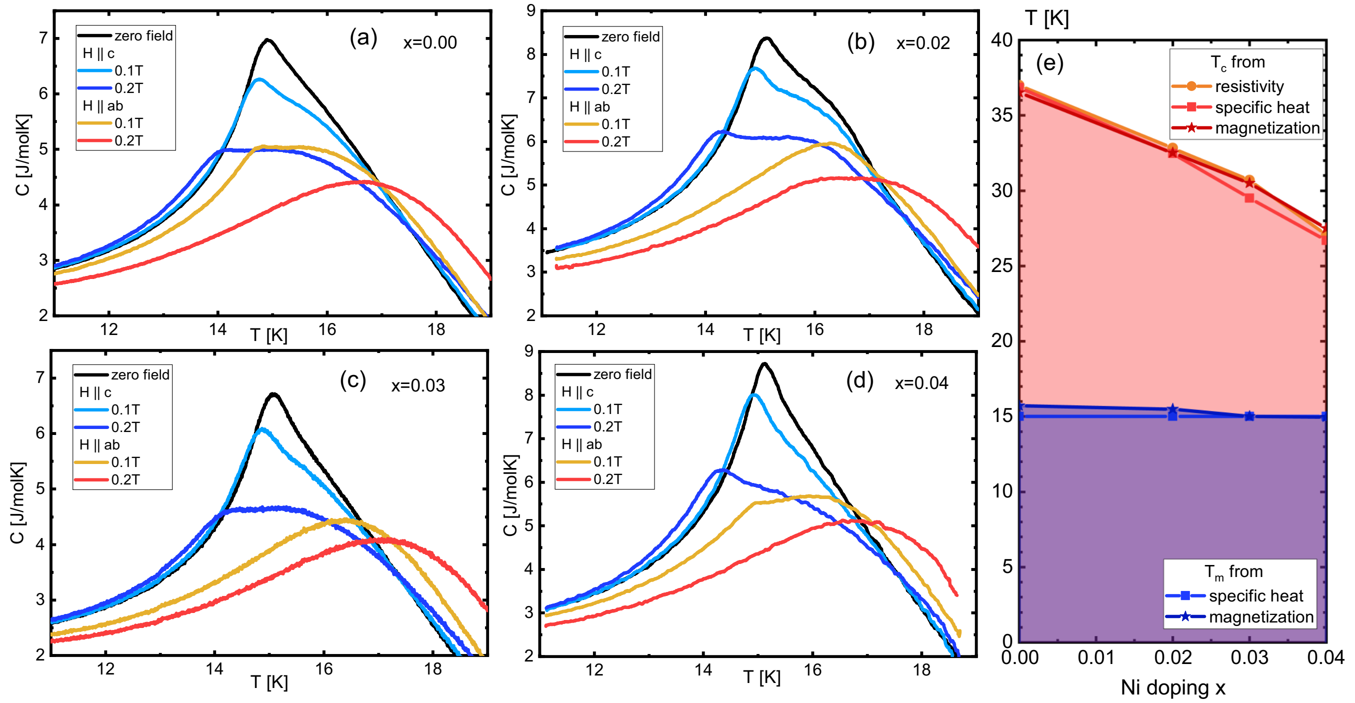

FIG. 8. Specific heat near the magnetic transition for 0% (a), 2% (b), 3% (c), and 4% (d) Ni doping. A 9-T background curve has been subtracted. The transition temperature $T_m = 15$ K, here the peak in C, appears unchanged upon Ni doping as does the shape of the transition. Small fields along the c axis shift the transition to lower temperatures while fields in plane transform the transition into a crossover that moves to higher temperatures. (e) Shows the phase diagram extracted from specific heat, magnetization, and resistivity for the magnetic and superconducting transitions in zero field upon increasing Ni doping.

the BCS coherence length $\xi(0) = 0.74\xi_0 = 0.76\hbar v_F/\Delta(0) \approx \hbar v_F/2.38k_BT_c$. This results in $H_{c2}(0) \propto T_{c2}^2/v_F^2$ and an upper critical field slope $dH_{c2}/dT_c \propto T_c/v_F^2$. Thus, assuming that changes in the electronic structure are not dominant (see above), the upper critical field and the slope of it indeed decrease with decreasing T_c, that is, with increasing Ni doping. The same conclusion would also be reached in the dirty limit, when the coherence length is given as $\xi(0) = 0.855(\xi_0 l)^{1/2}$ resulting in $H_{c2}(0) \propto T_c/v_F^2\tau$. Since $\rho \propto 1/\tau$ is proportional to T_c (with an offset), one again finds to leading order $H_{c2}(0) \propto T_{c2}^2$ and a slope that decreases with increasing Ni doping.

In order to gain insight into the nature of the magnetic transition, we performed detailed specific-heat measurements in the close vicinity of the transition. In zero field, the transition is characterized by a kink in the specific heat for all doping levels, a nonsingular behavior that was already observed for the undoped compound and identified as a BKT transition [23]. As noted above, the transition temperature of $T_m = 15$ K is largely unaffected by the Ni doping. Applying small fields along the c axis shifts the magnetic transition to lower temperatures while applying the field in the plane replaces the transition with a crossover. The similar field response of the specific heat of the doped samples (Fig. 8) and of the undoped samples (Ref. [23]), leads us to conclude that Ni-doped RbEuFe$_4$As$_4$, just as the stoichiometric compound, belongs to the universality class of the 2D XY model, with the Eu moments having an easy-plane anisotropy, strong ferromagnetic intralayer coupling, and very weak interlayer interactions leading to the BKT transition of the moments in the plane near $T_m = 15$ K. This transition will be suppressed to lower temperatures for fields along the c axis, and lifted to a broad crossover for fields in the plane as the latter destroys the rotational symmetry necessary for a BKT transition.

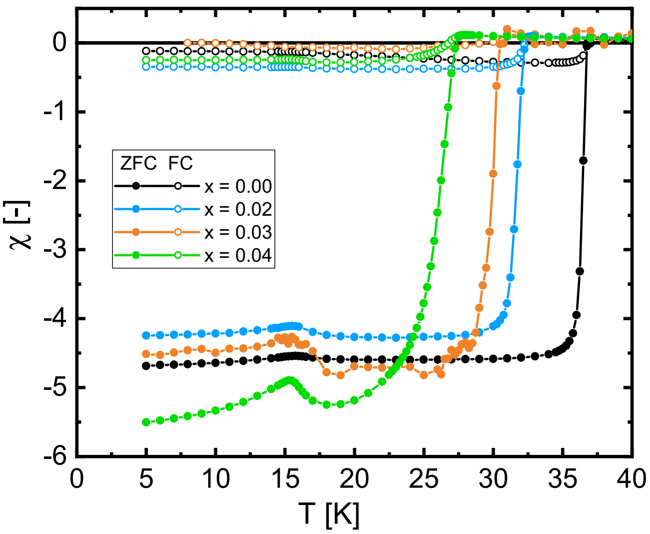

FIG. 9. The ZFC and FC magnetic susceptibilities of RbEu(Fe$_{1-x}$Ni$_x$)$_4$As$_4$ single crystals with $H = 1$ mT along the [001] direction. With increasing doping, the onset T_c shifts lower while the transitions remain parallel, indicating homogeneous doping. In this orientation, the diamagnetism masks most of the Eu magnetism.

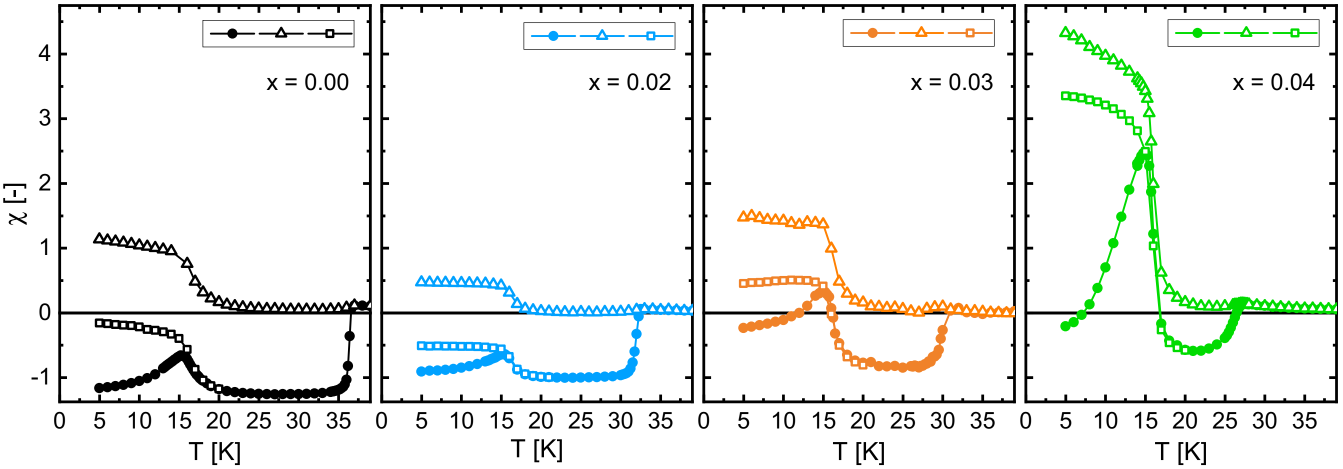

FIG. 10. The ZFC and FC magnetic susceptibilities of RbEu$(Fe_{1-x}Ni_x)_4As_4$ single crystals with $H = 1$ mT applied along the [110] direction. Solid circles mark ZFC, hollow triangles, FC. Hollow squares represent cooling in zero field, applying 10 mT, warming to 20 K, and then measuring FC.

D. Magnetization

We study the magnetic state of RbEu$(Fe_{1-x}Ni_x)_4As_4$ by measuring the zero-field-cooled (ZFC) and field-cooled (FC) temperature dependence of the magnetization in different applied fields as well as the field dependence of the magnetization at different temperatures with the field applied perpendicular or parallel to the c axis. Figure 9 shows ZFC and FC measurements of magnetic susceptibility, $\chi = M/H$, for $x = 0.00$, 0.02, 0.03, and 0.04 with $H = 10$G applied along [001]. Slight differences in demagnetization factors may cause variations in the absolute magnitude of susceptibility. As doping increases, the onset of diamagnetism, taken as T_c, monotonically decreases from 36.5 to 27.5 K, in agreement with the resistivity and the specific-heat data. Due to the platelike sample geometries, magnetization data for $H \parallel [001]$ contain large superconducting contributions, making the Eu magnetism difficult to discern in this geometry.

Applying magnetic fields along [110] decreases the contribution of diamagnetism, allowing for a more pronounced development of the Eu magnetism, as shown in Fig. 10. In the magnetization measurements, we find that T_m, defined as the peak in the ZFC susceptibility below T_c, is slightly suppressed from 15.3 to 15.0 K by low Ni doping. This is in rough agreement with the specific-heat data showing that the magnetic ordering temperature is essentially independent of Ni doping.

In higher fields, the magnetic susceptibility for FC measurements at all doping levels is qualitatively very similar to the undoped compound [22] as shown in Fig. 11. At 0.1 T we observe a large anisotropy in the low-temperature susceptibility with $\chi_{ab} \gg \chi_c$ under FC conditions where vortex pinning

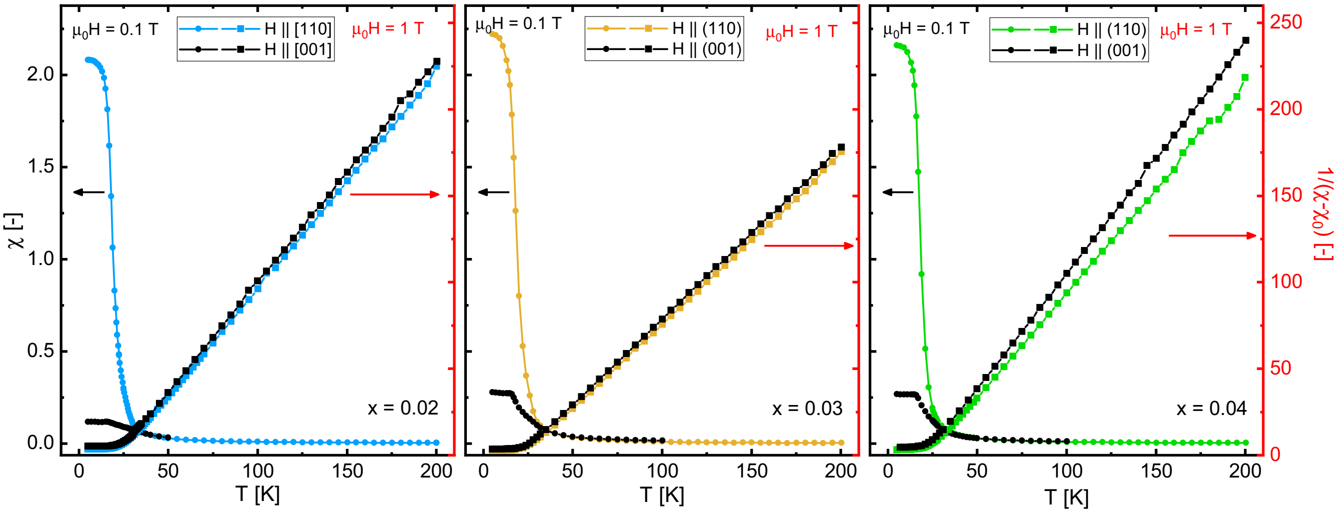

FIG. 11. Temperature dependence of field-cooled magnetic susceptibility measured upon warming in RbEu$(Fe_{1-x}Ni_x)_4As_4$ single crystals: (a) $x = 0.02$. (b) $x = 0.03$. (c) $x = 0.04$. For all panels, colored symbols represent $H \parallel [110]$, black symbols represent H $\parallel$ [001]. For $\mu_0 H = 0.1$ T, the large in-plane to out-of-plane anisotropy is present at all doping levels. The right-hand axis in each panel plots the inverse susceptibility measured for fields of 10 T; the low-temperature behavior is more isotropic, and the high-temperature (>50 K) data can be well described by Curie-Weiss behavior.

TABLE I. Properties of single crystals of $RbEu(Fe_{1-x}Ni_x)_4As_4$ derived from x-ray diffraction, resistivity, specific-heat, and magnetization measurements. Θ_C^{xy} denotes the Curie temperature for in-plane fields and Θ_C^z the one for fields along the c axis.

x $(-)$	c (Å)	T_C (K)	ρ @ T_c ($\mu\Omega$ cm)	$\Delta C/T_c$ (J/mol K^2)	μ_{eff} (μ_B/Eu)	Θ_C^{xy} (K)	Θ_C^z (K)	Θ_C^{xy}/Θ_C^z $(-)$	M_{sat} (μ_B/Eu)
0.00	13.3047	36.9	22	0.23	7.75	23.00	21.40	1.075	7.2
0.02	13.2911	32.5	54	0.19	7.87	23.18	21.94	1.057	6.4
0.03	13.2825	30.7	94	0.14	8.89	22.53	20.87	1.078	8.1
0.04	13.2733	26.9	139	0.12	7.97	22.84	21.04	1.086	6.5

effects are small. Thus, the strong easy-plane anisotropy of the Eu moments observed in the undoped compound is preserved with Ni doping. At 1 T and above 50 K the data are well described by a Curie-Weiss law $\chi(T) = \chi_0 + C/(T - \Theta_c)$, yielding $\Theta_c \approx 23$ K and an effective moment $\mu_{\mathrm{eff}} = 2.837C^{1/2}$ close to the expected Eu^{2+} effective moment of $\mu_{\mathrm{eff}} = g\mu_B\sqrt{S(S+1)} = 7.94\mu_{\mathrm{B}}/\mathrm{Eu}$ (with $g = 2$ and $S = \frac{7}{2}$) suggesting that these low levels of Ni doping do not substantially affect the Eu magnetic interactions as expected in numerical simulations [42]. As doping increases, the peak of the magnetic transition is almost unchanged showing that magnetism is essentially unaffected by Ni doping. Fit values are shown in Table I. The higher value of μ_{eff} found for $x = 0.03$ is likely due to surface $EuFe_2As_2$ phase on the sample, which would contribute twice as much Eu per volume as the 1144 phase would. The positive Curie-Weiss temperature values suggests predominantly ferromagnetic interactions between the Eu moments consistent with what has been seen in the undoped compound. Within a 2D Heisenberg model that includes in-plane versus out-of-plane spin anisotropy [23], the anisotropy of the Curie-Weiss temperatures between in-plane and out-of-plane fields is a measure of the anisotropy of the Eu spins. It is essentially unchanged upon Ni doping consistent with the data obtained at low temperatures.

The insets of Figs. 12(a)–12(f) show magnetization hysteresis loops measured at 5 K for in-plane and out-of-plane fields. The superposition of a hysteretic superconducting signal and a ferromagnetic-like signal is clearly seen, especially for H ∥ [001]. The large sample cross section and high critical current density for H ∥ [001] makes this an expected behavior. In comparison to the $x = 0.02$ and 0.04 samples, the $x = 0.03$ sample displays a lower superconducting hysteresis corresponding to weak pinning which suggests less disorder. Assuming that the superconducting hysteresis is symmetric about the equilibrium magnetization curve and that the magnetic hysteresis of the Eu spins is negligible as was

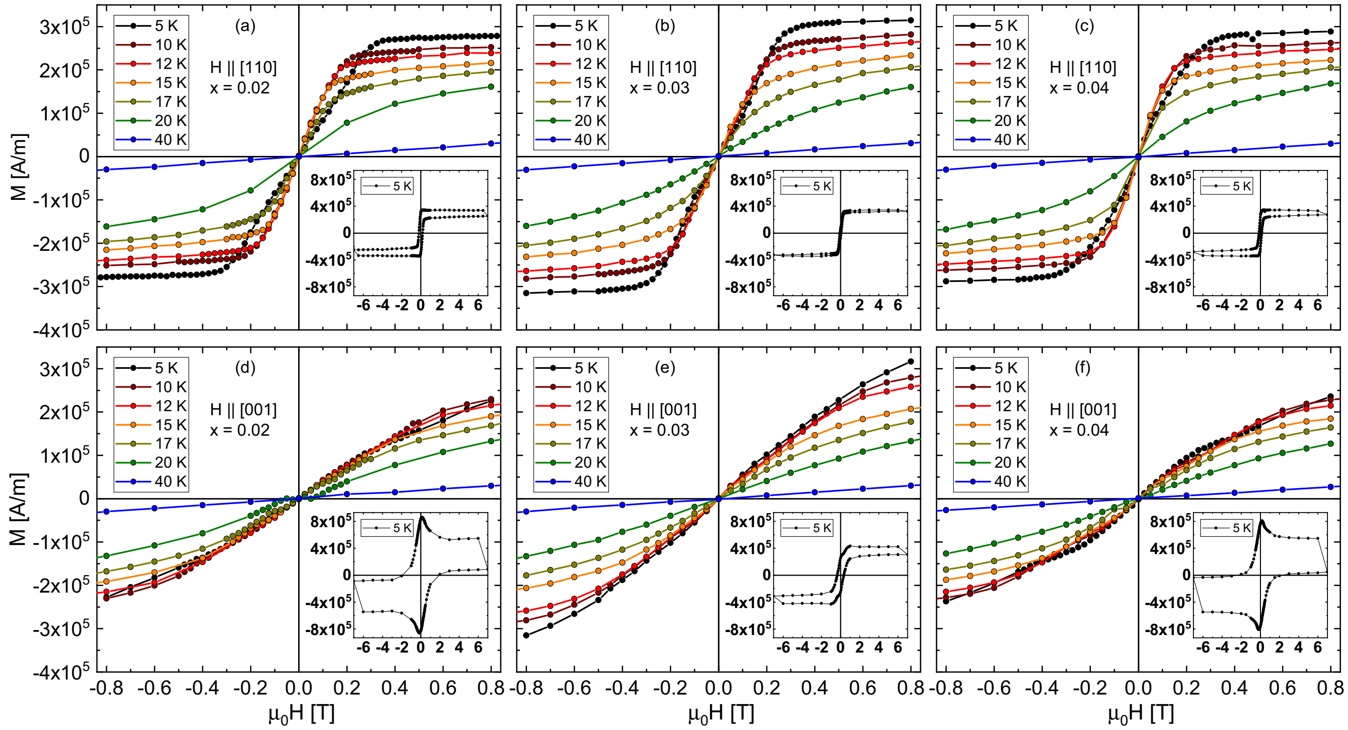

FIG. 12. Magnetization of the Eu sublattice vs applied field H ∥ [110] (a)–(c) and along H ∥ [001] (d)–(f) for different doping levels and at various temperatures. The insets show the as-measured magnetization hysteresis loops. At high fields, the saturation magnetization approaches ≈300 emu/cm^3, approximately that of the pristine material. In all measurements, the slope of the magnetization increases as T_m is approached from above, and decreases for $T < T_m$ as the magnetic lattice becomes stiffer.

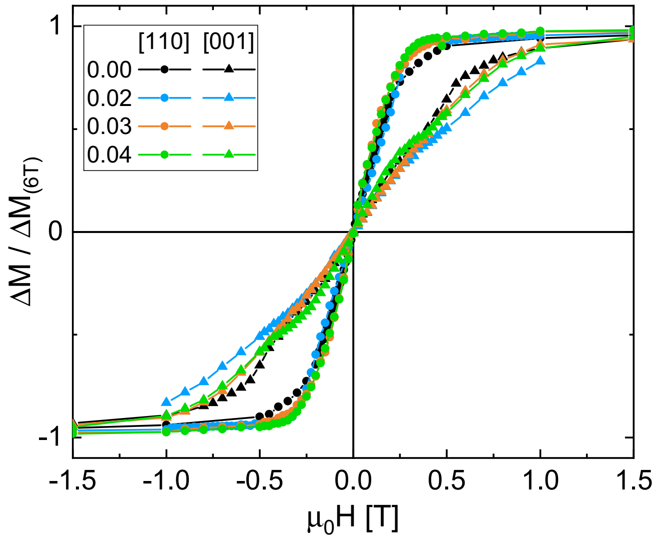

FIG. 13. Comparison of the symmetrized component, representing the ferromagnetic component, of the magnetic hysteresis of Ni-doped single crystals of $\mathrm{RbEu(Fe_{1-x}Ni_x)_4As_4}$ with H ∥ [110] (circles) and H ∥ [001] (triangles). Increasing the doping does not change the field necessary to collapse the Eu magnetic lattice.

found in the nonsuperconducting parent compound $\mathrm{EuFe_2As_2}$ [47], we determine the magnetization curve M(H) of the Eu spin sublattice as $M = (M_+ + M_-)/2$ where M_+ (M_-) is the magnetization measured in increasing (decreasing) applied field. The results are shown for multiple temperatures in the main panels of Figs. 12(a)–12(f). Above T_m, a Brillouin-type response is observed. The slopes of the magnetization curves grow as T_m is approached, then become slightly lower as T decreases and the magnetic lattice stiffens. For H ∥ [110] and H ∥ [001], the saturation magnetization reaches ≈300 emu/cm^3 (compare Table I) corresponding to $6.4\mu_B$/Eu, comparable to the expected full moment. Some excess moment was found for the $x = 0.03$ sample, that can again be attributed to an impurity $\mathrm{EuFe_2As_2}$ phase. Additionally, differences from the free moment value may arise from the approximation of the hysteresis model.

The 5 K Eu-sublattice magnetization curves for the three doping levels and a pristine sample in both field orientations are plotted together in Fig. 13. In order to minimize the effect of variations from varying degrees of hysteresis and from uncertainties in sample volume, we normalize each curve to its value at 6 T. There is no systematic change with doping of the saturation field in either orientation, with saturation fields of $H^{ab}_{\mathrm{sat}} \approx 0.21$ T and $H^{c}_{\mathrm{sat}} \approx 0.8$–1 T for all doping levels, consistent with the pronounced easy-plane magnetic anisotropy.

IV. CONCLUSION

We have studied the effect of up to 4% Ni doping on the Fe site in the magnetic superconductor $\mathrm{RbEuFe_4As_4}$ in specific-heat, resistivity, and magnetization measurements. We observe a clear suppression of the superconducting transition temperature T_c. Upon Ni doping, the resistivity curve shifts up in a parallel fashion, indicating a strong increase of the residual resistivity due to scattering by charged dopant atoms while the electronic structure appears largely unchanged. The observed step $\Delta C/T_c$ at the superconducting transition decreases strongly for increasing Ni doping in agreement with BNC scaling. The upper critical field slopes are reduced upon Ni doping for in-plane as well as out-of-plane fields, leading to a small reduction in the superconducting anisotropy. Specific-heat measurements of the magnetic transition reveal the same BKT behavior close to the transition temperature T_m for all doping levels, with the transition temperature essentially unchanged and the in-plane to out-of-plane anisotropy of Eu magnetism observed at small magnetic fields, is unaffected. All of these observations indicate a decoupling of the Eu magnetism from superconductivity and essentially no influence of Ni doping on the Eu magnetism in this compound. These findings are in line with recent first-principles calculations [42], indicating that the coupling between the Eu moments is mediated by the Ruderman-Kittel-Kasuya-Yosida (RKKY) interaction via the Fe-d_{z^2} orbitals which were found to be remarkably insensitive to Ni doping.

ACKNOWLEDGMENTS

This work was supported by the U. S. Department of Energy, Office of Science, Basic Energy Sciences, Materials Sciences and Engineering Division. K.W. acknowledges support from the Swiss National Science Foundation through the Early Postdoc. Mobility program.

---

[1] Y. Kamihara, T. Watanabe, M. Hirano, and H. Hosono, J. Am. Chem. Soc. **130**, 3296 (2008).
[2] M. Rotter, M. Tegel, and D. Johrendt, Phys. Rev. Lett. **101**, 107006 (2008).
[3] J. W. Lynn and P. Dai, Phys. C (Amsterdam) **469**, 469 (2009).
[4] D. C. Johnston, Adv. Phys. **59**, 803 (2010).
[5] G. R. Stewart, Rev. Mod. Phys. **83**, 1589 (2011).
[6] K. Tanabe and H. Hosono, Jpn. J. Appl. Phys. **51**, 010005 (2011).
[7] H. Hosono and K. Kuroki, Phys. C (Amsterdam) **514**, 399 (2015).
[8] Q. Si, R. Yu, and E. Abrahams, Nat. Rev. Mater **1**, 16017 (2016).
[9] Y. Bang and G. R. Stewart, J. Phys.: Condens. Matter **29**, 123003 (2017).
[10] N. Kurita, M. Kimata, K. Kodama, A. Harada, M. Tomita, H. S. Suzuki, T. Matsumoto, K. Murata, S. Uji, and T. Terashima, Phys. Rev. B **83**, 214513 (2011).
[11] F. Hardy, N. J. Hillier, C. Meingast, D. Colson, Y. Li, N. Barišić, G. Yu, X. Zhao, M. Greven, and J. S. Schilling, Phys. Rev. Lett. **105**, 167002 (2010).
[12] C. Meingast, F. Hardy, R. Heid, P. Adelmann, A. Böhmer, P. Burger, D. Ernst, R. Fromknecht, P. Schweiss, and T. Wolf, Phys. Rev. Lett. **108**, 177004 (2012).
[13] F. Hardy, A. E. Böhmer, L. de' Medici, M. Capone, G. Giovannetti, R. Eder, L. Wang, M. He, T. Wolf, P. Schweiss,

R. Heid, A. Herbig, P. Adelmann, R. A. Fisher, and C. Meingast, Phys. Rev. B **94**, 205113 (2016).

[14] W. T. Jin, Y. Xiao, S. Nandi, S. Price, Y. Su, K. Schmalzl, W. Schmidt, T. Chatterji, A. Thamizhavel, and T. Brückel, Phys. Rev. B **100**, 014503 (2019).

[15] A. Iyo, K. Kawashima, T. Kinjo, T. Nishio, S. Ishida, H. Fujihisa, Y. Gotoh, K. Kihou, H. Eisaki, and Y. Yoshida, J. Am. Chem. Soc. **138**, 3410 (2016).

[16] K. Kenji, K. Tatsuya, N. Taichiro, I. Shigeyuki, F. Hiroshi, G. Yoshito, K. Kunihiro, E. Hiroshi, Y. Yoshiyuki, and I. Akira, J. Phys. Soc. Jpn. **85**, 064710 (2016).

[17] Y. Liu, Y.-B. Liu, Q. Chen, Z.-T. Tang, W.-H. Jiao, Q. Tao, Z.-A. Xu, and G.-H. Cao, Science Bulletin **61**, 1213 (2016).

[18] Y. Liu, Y.-B. Liu, Z.-T. Tang, H. Jiang, Z.-C. Wang, A. Ablimit, W.-H. Jiao, Q. Tao, C.-M. Feng, Z.-A. Xu, and G.-H. Cao, Phys. Rev. B **93**, 214503 (2016).

[19] W. R. Meier, T. Kong, U. S. Kaluarachchi, V. Taufour, N. H. Jo, G. Drachuck, A. E. Böhmer, S. M. Saunders, A. Sapkota, A. Kreyssig, M. A. Tanatar, R. Prozorov, A. I. Goldman, F. F. Balakirev, A. Gurevich, S. L. Bud'ko, and P. C. Canfield, Phys. Rev. B **94**, 064501 (2016).

[20] W. Liu, L. Cao, S. Zhu, L. Kong, G. Wang, M. Papaj, P. Zhang, Y. Liu, H. Chen, G. Li, F. Yang, T. Kondo, S. Du, G. Cao, S. Shin, L. Fu, Z. Yin, H.-J. Gao, and H. Ding, arXiv:1907.00904.

[21] J.-K. Bao, K. Willa, M. P. Smylie, H. Chen, U. Welp, D. Y. Chung, and M. G. Kanatzidis, Cryst. Growth Des. **18**, 3517 (2018).

[22] M. P. Smylie, K. Willa, J.-K. Bao, K. Ryan, Z. Islam, H. Claus, Y. Simsek, Z. Diao, A. Rydh, A. E. Koshelev, W.-K. Kwok, D. Y. Chung, M. G. Kanatzidis, and U. Welp, Phys. Rev. B **98**, 104503 (2018).

[23] K. Willa, R. Willa, J.-K. Bao, A. E. Koshelev, D. Y. Chung, M. G. Kanatzidis, W.-K. Kwok, and U. Welp, Phys. Rev. B **99**, 180502(R) (2019).

[24] M. P. Smylie, A. E. Koshelev, K. Willa, R. Willa, W.-K. Kwok, J.-K. Bao, D. Y. Chung, M. G. Kanatzidis, J. Singleton, F. F. Balakirev, H. Hebbeker, P. Niraula, E. Bokari, A. Kayani, and U. Welp, Phys. Rev. B **100**, 054507 (2019).

[25] H. S. Jeevan, D. Kasinathan, H. Rosner, and P. Gegenwart, Phys. Rev. B **83**, 054511 (2011).

[26] K. Japil, P. Jihwey, K. C. Sung, D. K. Ki, P. Sang-Youn, H. J. Yoon, J. P. Yong, Y. K. Tae, H. Kun-Pyo, L. Chang-Hee, K. Ju-Young, C. Beong-Ki, B. L. Ki, and K. Heon-Jung, J. Phys. Soc. Jpn. **79**, 114708 (2010).

[27] S. Zapf and M. Dressel, Rep. Prog. Phys. **80**, 016501 (2017).

[28] S. Nandi, W. T. Jin, Y. Xiao, Y. Su, S. Price, D. K. Shukla, J. Strempfer, H. S. Jeevan, P. Gegenwart, and T. Brückel, Phys. Rev. B **89**, 014512 (2014).

[29] Y. Xiao, Y. Su, M. Meven, R. Mittal, C. M. N. Kumar, T. Chatterji, S. Price, J. Persson, N. Kumar, S. K. Dhar, A. Thamizhavel, and T. Brueckel, Phys. Rev. B **80**, 174424 (2009).

[30] K. Iida, Y. Nagai, S. Ishida, M. Ishikado, N. Murai, A. D. Christianson, H. Yoshida, Y. Inamura, H. Nakamura, A. Nakao, K. Munakata, D. Kagerbauer, M. Eisterer, K. Kawashima, Y. Yoshida, H. Eisaki, and A. Iyo, Phys. Rev. B **100**, 014506 (2019).

[31] I. Zahir *et al.* (unpublished).

[32] Y. Liu, Y.-B. Liu, Y.-L. Yu, Q. Tao, C.-M. Feng, and G.-H. Cao, Phys. Rev. B **96**, 224510 (2017).

[33] K. Kawashima, S. Ishida, K. Oka, H. Kito, N. Takeshita, H. Fujihisa, Y. Gotoh, K. Kihou, H. Eisaki, Y. Yoshida, and A. Iyo, J. Phys.: Conf. Ser. **969**, 012027 (2018).

[34] D. E. Jackson, D. VanGennep, W. Bi, D. Zhang, P. Materne, Y. Liu, G.-H. Cao, S. T. Weir, Y. K. Vohra, and J. J. Hamlin, Phys. Rev. B **98**, 014518 (2018).

[35] Z. Devizorova and A. Buzdin, Phys. Rev. B **100**, 104523 (2019).

[36] A. E. Koshelev, Phys. Rev. B **100**, 224503 (2019).

[37] V. K. Vlasko-Vlasov, A. E. Koshelev, M. Smylie, J. K. Bao, D. Y. Chung, M. G. Kanatzidis, U. Welp, and W. K. Kwok, Phys. Rev. B **99**, 134503 (2019).

[38] S. L. Bud'ko, N. Ni, and P. C. Canfield, Phys. Rev. B **79**, 220516(R) (2009).

[39] Y. Bang and G. R. Stewart, New J. Phys. **18**, 023017 (2016).

[40] S. Tagliati, V. M. Krasnov, and A. Rydh, Rev. Sci. Instrum. **83**, 055107 (2012).

[41] K. Willa, Z. Diao, D. Campanini, U. Welp, R. Divan, M. Hudl, Z. Islam, W.-K. Kwok, and A. Rydh, Rev. Sci. Instrum. **88**, 125108 (2017).

[42] C. Xu, Q. Chen, and C. Cao, Commun. Phys. **2**, 2399 (2019).

[43] U. B. Paramanik, D. Das, R. Prasad, and Z. Hossain, J. Phys.: Condens. Matter **25**, 265701 (2013).

[44] A. E. Koshelev, K. Willa, R. Willa, M. P. Smylie, J.-K. Bao, D. Y. Chung, M. G. Kanatzidis, W.-K. Kwok, and U. Welp, Phys. Rev. B **100**, 094518 (2019).

[45] P. J. Hirschfeld, M. M. Korshunov, and I. I. Mazin, Rep. Prog. Phys. **74**, 124508 (2011).

[46] K. Willa, R. Willa, K. W. Song, G. D. Gu, J. A. Schneeloch, R. Zhong, A. E. Koshelev, W.-K. Kwok, and U. Welp, Phys. Rev. B **98**, 184509 (2018).

[47] S. Jiang, Y. Luo, Z. Ren, Z. Zhu, C. Wang, X. Xu, Q. Tao, G. Cao, and Z. Xu, New J. Phys. **11**, 025007 (2009).